

High-Efficiency Three-Stroke Quantum Isochoric Heat Engine: From Infinite Potential Wells to Magic-Angle Twisted Bilayer Graphene

Hadi Mohammed Soufy^{1, 2, *} and Colin Benjamin^{1, 2, †}

¹*School of Physical Sciences, National Institute of Science Education and Research, HBNI, Jatni-752050, India*

²*Homi Bhabha National Institute, Training School Complex, Anushakti Nagar, Mumbai, 400094, India*

We introduce a three-stroke quantum isochoric cycle that functions as a heat engine operating between two thermal reservoirs. Implemented for a particle confined in a one-dimensional infinite potential well, the cycle's performance is benchmarked against the classical three-stroke triangular and isochoric engines. We find that the quantum isochoric cycle achieves a higher efficiency than both classical counterparts and also surpasses the efficiency of the recently proposed three-stroke quantum isoenergetic cycle. Owing to its reduced number of strokes, the design substantially lowers control complexity in nanoscale thermodynamic devices, offering a more feasible route to experimental realization compared to conventional four-stroke architectures. We further evaluate the cycle in graphene-based systems under an external magnetic field, including monolayer graphene (MLG), AB-stacked bilayer graphene (BLG), and twisted bilayer graphene (TBG) at both magic and non-magic twist angles. Among these platforms, magic-angle twisted bilayer graphene (MATBG) attains the highest efficiency at fixed work output, highlighting its promise for quantum thermodynamic applications.

I. INTRODUCTION

The intersection of quantum mechanics and thermodynamics has led to a rapidly developing field focused on microscopic quantum thermodynamic devices (QTDs) [1–3]. Operating at the scale of individual atoms and engineered quantum systems, these devices challenge classical intuition by revealing how coherence, discreteness, and quantum statistics influence energy-conversion processes [4–7]. Over the past decade, QTDs have been realized experimentally in a wide range of platforms, including trapped ions [8, 9], superconducting circuits [10], nitrogen-vacancy centers in diamond [11], ultracold atomic ensembles [12], and optomechanical systems [13]. These breakthroughs demonstrate that thermodynamic cycles, traditionally associated with macroscopic engines, can be meaningfully implemented at the quantum scale, often with enhanced control and access to operational regimes without classical analogues. Designing such machines requires balancing heat exchange and work extraction across discrete thermodynamic strokes [14, 15], with the number and nature of the strokes dictating how energy flow is orchestrated. Understanding how each stroke shapes performance is therefore essential for harnessing the capabilities of quantum materials. Although four-stroke cycles form the conventional framework for analyzing work and efficiency, many experimental platforms struggle to realize all four operations with high precision due to decoherence, noise, and limited control resources [16, 17]. Reducing the cycle to three strokes provides a practical alternative that retains essential thermodynamic features while significantly

simplifying implementation, making three-stroke models both conceptually insightful and experimentally relevant [18, 19].

In this work, we begin by analyzing two classical three-stroke engines, the triangular cycle and the isochoric cycle, to establish a baseline for comparison. We then introduce a quantum analogue by considering a particle confined in a one-dimensional infinite potential well (IPW) and implementing two distinct quantum three-stroke cycles: a quantum isochoric cycle operating between two thermal baths, and a quantum isoenergetic cycle, originally proposed in Ref. [20], which operates by maintaining constant internal energy while interacting with a single bath. By systematically comparing their thermodynamic behavior, we show that the quantum isochoric cycle attains both higher efficiency and greater work output than the quantum isoenergetic cycle under identical operating conditions. Building on this insight, we extend our analysis to graphene-based platforms: monolayer graphene (MLG), AB Bernal-stacked bilayer graphene (BLG), and twisted bilayer graphene (TBG) at both magic and non-magic twist angles, in the presence of a perpendicular magnetic field. Implementing the proposed quantum isochoric cycle in these systems allows us to evaluate and compare their performance as quantum heat engines.

Section II summarizes the thermodynamic foundations relevant to our analysis, including the conditions for feasibility of a cycle and the operational regimes of quantum heat engines. The specific cycles investigated in this work are then introduced in the subsequent subsections: Section IIA reviews the classical triangular cycle; Section IIB presents the classical isochoric cycle; Section IIC details the proposed three-stroke quantum isochoric cycle; and Section IID discusses the three-stroke quantum isoenergetic cycle. For each case, we describe the implementa-

* hm.soufy@niser.ac.in

† colin.nano@gmail.com

tion for a particle in an IPW, analyze compliance with the thermodynamic laws, and compare their performance metrics. Section III provides the theoretical background for graphene-based systems—MLG, BLG, and TBG at various twist angles—under an external magnetic field, while Section IIIA applies the quantum isochoric cycle to these platforms. Our main results and comparative analysis are presented in Section IV, followed by concluding remarks and potential experimental realizations in Section V.

II. THERMODYNAMIC CYCLE

To understand the performance of a system as a thermodynamic device, we analyze its behavior over a complete thermodynamic cycle. A cycle consists of a series of distinct thermodynamic strokes, that finally return the system to its initial state. The net work output and efficiency, which quantify the device's utility, are derived from the heat exchanged with the thermal reservoirs during these strokes [4, 14, 15, 21]. For a thermodynamic stroke, the first law of thermodynamics states,

$$\Delta U = Q - W, \quad (1)$$

where Q is the heat supplied to the system, W is the work done by the system and ΔU is the internal energy change. At the end of a cycle, $\Delta U = 0$; hence,

$$W_1 + W_2 + \dots = W = Q_1 + Q_2 + \dots \quad (2)$$

W_1, W_2, \dots and Q_1, Q_2, \dots are the work and heat exchanged in the individual thermodynamic strokes. For a system undergoing a thermodynamic cycle across two reservoirs at temperatures T_h and T_c , the heat exchanged with them is denoted by Q_{hot} and Q_{cold} , respectively. Eq. (2) then reduces to,

$$W = Q_{\text{hot}} + Q_{\text{cold}}. \quad (3)$$

The second law of thermodynamics requires total entropy change ΔS_{tot} over a cycle be non-negative, which is a necessary condition for physical realizability [4, 21, 22]. For a system undergoing a thermodynamic stroke while coupled to baths, this is expressed as,

$$\Delta S_{\text{tot}} = \Delta S_{\text{sys}} + \Delta S_{\text{bath}} \geq 0, \quad (4)$$

Here, ΔS_{sys} denotes the entropy change of the system, and ΔS_{bath} corresponds to that of the baths during the stroke. For a reversible process $\Delta S_{\text{tot}} = 0$. For a system undergoing a thermodynamic cycle, which may be reversible or irreversible, between two heat baths at temperatures T_h and T_c ($T_h > T_c$) [4, 22], we have,

$$\Delta S_{\text{sys}} = 0, \quad \text{and} \quad \Delta S_{\text{bath}} = -\frac{Q_{\text{hot}}}{T_h} - \frac{Q_{\text{cold}}}{T_c},$$

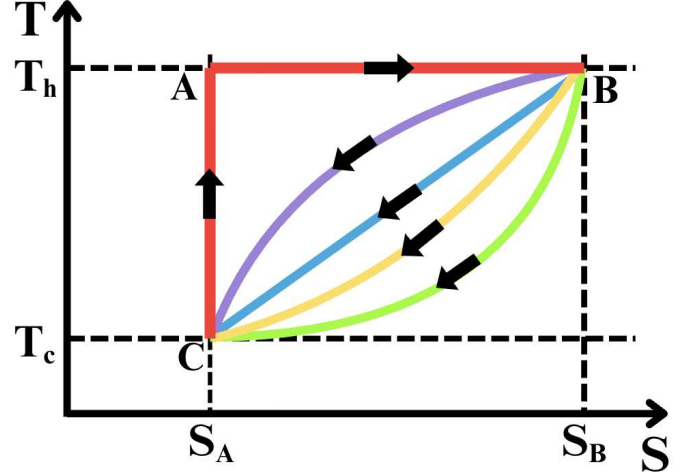


FIG. 1: Entropy - Temperature (T-S) diagrams for three thermodynamic cycles. Shown are: the classical triangular cycle $A \xrightarrow{\text{Blue}} B \xrightarrow{\text{Yellow}} C \xrightarrow{\text{Green}} A$ [25], the classical isochoric cycle $A \xrightarrow{\text{Yellow}} B \xrightarrow{\text{Green}} C \xrightarrow{\text{Blue}} A$, the quantum isochoric cycle $A \xrightarrow{\text{Green}} B \xrightarrow{\text{Blue}} C \xrightarrow{\text{Yellow}} A$, and the quantum isoenergetic cycle $A \xrightarrow{\text{Purple}} B \xrightarrow{\text{Blue}} C \xrightarrow{\text{Yellow}} A$ [20]. The classical triangular, classical isochoric and quantum isochoric cycles operate between two baths at fixed temperatures T_h and T_c , while the quantum isoenergetic cycle operates with a single bath at T_h , where the effective cold temperature T_c is not fixed but is determined by other parameters.

$$\text{Thus, } \Delta S_{\text{tot}} = -\frac{Q_{\text{hot}}}{T_h} - \frac{Q_{\text{cold}}}{T_c} \geq 0, \quad (5)$$

$$\text{which leads to the condition: } \frac{Q_{\text{hot}}}{T_h} + \frac{Q_{\text{cold}}}{T_c} \leq 0. \quad (6)$$

A heat engine is characterized by $W > 0$, $Q_{\text{hot}} > 0$, and $Q_{\text{cold}} < 0$, which corresponds to heat Q_{hot} being absorbed from the hot bath and Q_{cold} being rejected to the cold bath while performing work W [23, 24].

A. Three-Stroke Classical Triangular Cycle

In Fig. 1, $A \xrightarrow{\text{Blue}} B \xrightarrow{\text{Blue}} C \xrightarrow{\text{Blue}} A$ illustrates three-stroke triangular cycle. It consists of an isothermal stroke ($A \rightarrow B$), an adiabatic stroke ($C \rightarrow A$), and an irreversible stroke that connects the endpoints of the first two ($B \xrightarrow{\text{Blue}} C$) [21, 25]. For such a cycle, the performance coefficients depend solely on the temperature gradient between the thermal baths and is irreversible [21, 25] (see, Eq.(11)).

The system exchanges heat Q_{hot} with the hot bath during the isothermal stroke and heat Q_{cold} at the end of the irreversible stroke. The system is then brought back to its initial state by an adiabatic process. Q_{hot} corresponds to

the area under line AB, Q_{cold} is the negative of the area under blue line BC. Thus,

$$Q_{\text{hot}} = T_h(S_B - S_A), \quad Q_{\text{cold}} = \frac{1}{2}(T_h + T_c)(S_A - S_B), \quad (7)$$

and work done W_{CT} is the area of the cycle ABC (with the blue BC line),

$$W_{\text{CT}} = \frac{1}{2}(T_h - T_c)(S_B - S_A) = \frac{W_c}{2}, \quad (8)$$

where, W_c is the work done during a Carnot cycle operating between temperatures T_h and T_c . For N atoms of a classical ideal gas, work done during a Carnot cycle (W_c), is given by [21, 26],

$$W_c = \frac{Nk_B}{\gamma - 1} (T_h - T_c) \ln \left(\frac{T_h}{T_c} \right), \quad (9)$$

where γ is the specific heat capacity ratio and k_B is Boltzmann constant. For a single ($N = 1$) monoatomic ideal gas ($\gamma = \frac{5}{3}$), the work done in the triangular cycle (W_{CT}) from Eqs.(8) and (9) is then given by,

$$W_{\text{CT}} = \frac{3k_B}{4} (T_h - T_c) \ln \left(\frac{T_h}{T_c} \right). \quad (10)$$

At the end of the cycle using Eq.(7), Eq. (5) becomes,

$$\Delta S_{\text{sys}} = 0, \quad \text{and} \quad \Delta S_{\text{tot}} = \Delta S_{\text{bath}} = -\frac{Q_{\text{hot}}}{T_h} - \frac{Q_{\text{cold}}}{T_c}, \quad (11)$$

$$\Delta S_{\text{tot}} = (S_A - S_B) + (S_B - S_A) \frac{T_h + T_c}{2T_c} = (S_B - S_A) \frac{T_h - T_c}{2T_c}.$$

The second law is not violated if Q_{hot} and Q_{cold} obey the condition Eq. (6),

$$\frac{Q_{\text{hot}}}{T_h} + \frac{Q_{\text{cold}}}{T_c} = (S_A - S_B) \frac{T_h - T_c}{2T_c} \leq 0. \quad (12)$$

Thus, the classical triangular does not violate the second law if $S_A \leq S_B$, which gives us $W \geq 0$, $Q_{\text{hot}} \geq 0$, and $Q_{\text{cold}} \leq 0$, therefore the triangular cycle can only operate as a heat engine. The efficiency of the classical triangular cycle as a heat engine is then given as,

$$\eta_{\text{CT}} = \frac{W_{\text{CT}}}{Q_{\text{hot}}} = \frac{T_h - T_c}{2T_h} = \frac{\eta_c}{2} \quad (13)$$

where $\eta_c = 1 - \frac{T_c}{T_h}$, is the Carnot efficiency. From Eqs. (8) and (13) we notice that the work done and efficiency of the classical triangular cycle is half that of Carnot cycle.

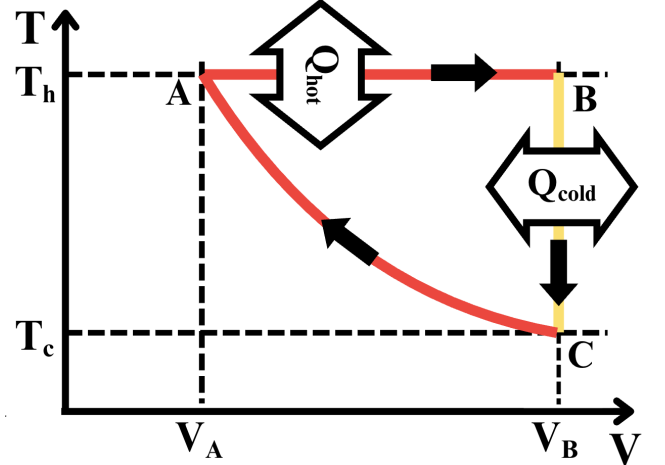


FIG. 2: Volume - Temperature diagram of ideal gas during a three-stroke classical isochoric cycle. Stroke $A \rightarrow B$ is the isothermal stroke, $B \xrightarrow{\text{Yellow}} C$ is the isochoric stroke, and $C \rightarrow A$ is the adiabatic stroke.

B. Three-Stroke Classical Isochoric Cycle

Fig. 2 depicts an ideal gas undergoing a three-stroke classical isochoric cycle. Stroke $A \rightarrow B$ is isothermal, where the system at temperature T_h and volume V_A expands to volume V_B while maintaining equilibrium with the hot bath at temperature T_h . During this process, the system exchanges heat Q_{hot} with the hot bath. Stroke $B \xrightarrow{\text{Yellow}} C$ is the classical isochoric process, where the volume is kept fixed at V_B as the system cools to temperature T_c of the cold bath. No work is done during this stroke, and the change in internal energy is entirely due to heat exchange Q_{cold} with the cold bath. Finally, in stroke $C \rightarrow A$, the system returns to its initial state through an adiabatic process, where no heat is exchanged and only work is performed. Using standard thermodynamic relations, we compute the heat exchanged with the hot and cold baths. For a classical isothermal process, the internal energy remains constant. Thus, from Eq. (1), we obtain [21, 26],

$$Q_{\text{hot}} = W_{\text{Isothermal}} = Nk_B T_h \ln \frac{V_B}{V_A}, \quad (14)$$

where N is the number of atoms and k_B is the Boltzmann constant. For a classical isochoric process, no work is exchanged. Therefore, from Eq. (1), we obtain [26],

$$Q_{\text{cold}} = \Delta U = C_v(T_c - T_h) = \frac{Nk_B(T_c - T_h)}{\gamma - 1}, \quad (15)$$

where C_v is the molar specific heat capacity at constant volume and γ is the specific heat capacity ratio. The adiabatic

stroke $C \rightarrow A$ yields the relation [21, 26],

$$T_c V_B^{\gamma-1} = T_h V_A^{\gamma-1} \Rightarrow \frac{V_B}{V_A} = \left(\frac{T_h}{T_c} \right)^{\frac{1}{\gamma-1}}. \quad (16)$$

To verify the feasibility of the cycle, we substitute Eqs. (14) and (15) into Eq. (6),

$$\begin{aligned} \frac{Q_{\text{hot}}}{T_h} + \frac{Q_{\text{cold}}}{T_c} &= \frac{Nk_B T_h \ln \frac{T_h}{T_c}}{T_h(\gamma-1)} + \frac{Nk_B (T_c - T_h)}{T_c(\gamma-1)} \\ &= \frac{Nk_B}{\gamma-1} \left(\ln \frac{T_h}{T_c} - \frac{T_h}{T_c} + 1 \right) \leq 0. \end{aligned} \quad (17)$$

For a stable thermodynamic system, $\gamma > 1$, and the quantity $\left(\ln \frac{T_h}{T_c} - \frac{T_h}{T_c} + 1 \right)$ is always negative when $T_h > T_c$. Hence, the cycle is consistent with the second law. For one complete cycle,

$$\begin{aligned} \Delta S_{\text{sys}} &= 0, \quad \text{and} \quad \Delta S_{\text{tot}} = \Delta S_{\text{bath}} = -\frac{Q_{\text{hot}}}{T_h} - \frac{Q_{\text{cold}}}{T_c}, \\ \Delta S_{\text{tot}} &= \frac{Nk_B}{\gamma-1} \left(\frac{T_h}{T_c} - \ln \frac{T_h}{T_c} - 1 \right) \geq 0. \end{aligned} \quad (18)$$

Using Eqs. (14), (15), and (16), the total work exchanged during the complete classical isochoric cycle (W_{CI}) for a single ($N = 1$) monoatomic ($\gamma = \frac{5}{3}$) ideal gas is,

$$\begin{aligned} W_{\text{CI}} &= Q_{\text{hot}} + Q_{\text{cold}} = \frac{Nk_B \left(T_h \ln \frac{T_h}{T_c} + (T_c - T_h) \right)}{\gamma-1} \\ &= \frac{3}{2} k_B \left(T_h \ln \frac{T_h}{T_c} + (T_c - T_h) \right). \end{aligned} \quad (19)$$

The efficiency (η_{CI}) of the classical three-stroke isochoric cycle operating as a heat engine is then given as,

$$\begin{aligned} \eta_{\text{CI}} &= \frac{W_{\text{CI}}}{Q_{\text{hot}}} = 1 + \frac{\frac{Nk_B(T_c - T_h)}{\gamma-1}}{\frac{Nk_B T_h \ln \frac{T_h}{T_c}}{\gamma-1}}, \\ &= 1 + \frac{T_c - T_h}{T_h \ln \frac{T_h}{T_c}} = 1 + \frac{\eta_c}{\ln(1 - \eta_c)}, \end{aligned} \quad (20)$$

where $\eta_c = 1 - \frac{T_c}{T_h}$ is the Carnot efficiency. The efficiency of the classical isochoric cycle lies between those of the Carnot and classical triangular cycles, i.e., $\eta_{\text{CT}} \leq \eta_{\text{CI}} \leq \eta_c$. In the following section, we introduce quantum three-stroke cycles where the second stroke is replaced by either a quantum isoenergetic or quantum isochoric process. The efficiency and work output for the classical triangular and classical isochoric cycles are compared with the quantum isochoric and quantum isoenergetic cycles in Figs. 4 and 6 in Sections II B and II C.

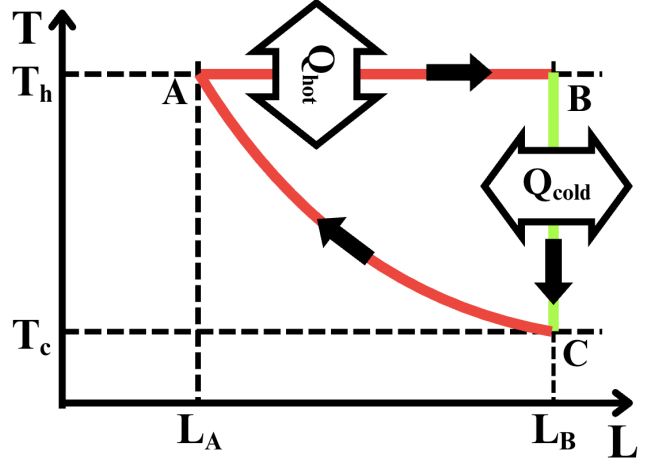


FIG. 3: Length - Temperature diagram of the particle in an IPW during a three-stroke quantum isochoric cycle. Stroke $A \rightarrow B$ is the isothermal stroke, $B \xrightarrow{\text{Green}} C$ is the quantum isochoric stroke, and $C \rightarrow A$ is the adiabatic stroke.

C. Three-Stroke Quantum Isochoric Cycle for Quantum Particle in an Infinite Potential Well

We consider a particle in a 1D IPW of variable length L , operating as a three-stroke quantum isochoric thermodynamic cycle, as depicted in Figs. 1 and 3 ($A \rightarrow B \xrightarrow{\text{Green}} C \rightarrow A$). This cycle operates between two thermal baths at temperatures T_h and T_c ($T_h > T_c$), and consists of an isothermal stroke ($A \rightarrow B$), followed by a quantum isochoric stroke ($B \xrightarrow{\text{Green}} C$), and finally an adiabatic stroke ($C \rightarrow A$). The quantized energy levels of a quantum particle in the 1D IPW are given by [27, 28],

$$E_n(L) = \frac{n^2 \hbar^2 \pi^2}{2mL^2}, \quad (21)$$

where m is the particle mass (here taken to be the electron mass). For a system in thermal equilibrium at temperature T , with energy eigenvalues E_n and corresponding eigenstates $|n\rangle$, the thermal state ($\rho(L, T)$) is given by [4, 14, 15],

$$\begin{aligned} \rho(L, T) &= \sum_n p_n |n\rangle \langle n|, \quad \text{with} \quad p_n(L, T) = \frac{e^{-\beta E_n(L)}}{Z(L, T)}, \\ \text{and} \quad Z(L, T) &= \sum_n e^{-\beta E_n(L)}, \end{aligned} \quad (22)$$

where $p_n(L, T)$ are the occupation probabilities, $Z(L, T)$ is the partition function and $\beta = \frac{1}{k_B T}$, where k_B is the Boltzmann constant. In this framework, temperature T is defined as the statistical parameter that establishes the system's equilibrium energy distribution through the Boltzmann distribution [14, 29]. For all thermodynamic cycles

considered in this paper, this definition is consistently applied. During the isothermal stroke, the system remains in a Boltzmann state at T_h . It then relaxes to a Boltzmann state at T_c during the isochoric stroke. Finally, the adiabatic stroke returns the system quasi-statically to its initial Boltzmann state at T_h . Throughout all strokes, the system remains in a thermal state, ensuring that the temperature is well-defined at every stage. Once the thermal state is known, we can calculate other thermodynamic quantities such as entropy $S = -k_B \sum_n p_n \ln(p_n)$ and internal energy $U = \sum_n p_n E_n$.

The quantum nature here arises solely from the discrete energy levels of the system, with the system described by the thermal state of Eq.(22), at all points in the cycle. Since this state possesses no off-diagonal elements in the energy eigenbasis, quantum coherence is absent by design, as also studied in Refs. [14, 29, 30]. In this idealized, quasi-static limit, coherence does not play a role, the quantum adiabatic stroke is performed slowly enough to avoid transitions, preserving the diagonal, thermal structure of the state, and the heat exchange strokes maintain perfect, instantaneous equilibrium with their respective baths. The thermodynamic performance, including efficiency and work output, are governed solely by the discrete energy levels and the populations of these discrete energy levels.

For infinitesimal transformations, from Eq. (1), we obtain,

$$Q = \sum_n E_n(L) dp_n, \quad W = - \sum_n p_n(L, T) dE_n \quad (23)$$

• **Stroke A → B (Isothermal):** The system is coupled to the hot bath at temperature T_h . The well length expands from L_A to L_B at constant temperature. Heat exchanged during this process Q_{hot} is given by Eq.(23),

$$Q_{\text{hot}} = \sum_n \int_{L_A}^{L_B} E_n(L) \frac{\partial p_n(L, T)}{\partial L} dL, \quad (24)$$

which reduces to, (see, Appendix A),

$$Q_{\text{hot}} = T_h [S_B(L_B, T_h) - S_A(L_A, T_h)]. \quad (25)$$

• **Stroke B $\xrightarrow{\text{Green}}$ C (Quantum isochoric):** The well length is fixed at L_B as the system thermalizes with the cold bath at temperature T_c . This gives us the condition,

$$E_n^B(L_B) = E_n^C(L_B). \quad (26)$$

No work is performed, and heat Q_{cold} can be found using Eq.(23), as,

$$Q_{\text{cold}} = \sum_n E_n^B(L_B) [p_n^C(L_B, T_c) - p_n^B(L_B, T_h)]. \quad (27)$$

• **Stroke C → A (Adiabatic):** The system is brought back to its initial state adiabatically. This enforces the entropy-matching condition that determines the initial length L_A ,

$$S_C(L_B, T_c) = S_A(L_A, T_h), \quad (28)$$

since the energy levels of particle in an IPW obey the energy scaling condition, (i.e $\frac{E_n(L)}{E_m(L)} = \text{constant}$, for all n, m) [14, 29], we obtain a stricter condition for Eq.(28),

$$p_n^A(L_A, T_h) = p_n^C(L_B, T_c), \quad \forall n. \quad (29)$$

Now for some arbitrary energy levels: n, m ($n \neq m$), we have,

$$\begin{aligned} \frac{p_n^A(L_A, T_h)}{p_m^A(L_A, T_h)} &= \frac{p_n^C(L_B, T_c)}{p_m^C(L_B, T_c)} \Rightarrow \frac{e^{-\beta_h E_n(L_A)}}{e^{-\beta_h E_m(L_A)}} = \frac{e^{-\beta_c E_n(L_B)}}{e^{-\beta_c E_m(L_B)}}, \\ e^{-\beta_h \frac{\hbar^2 \pi^2}{2mL_A^2} (n^2 - m^2)} &= e^{-\beta_c \frac{\hbar^2 \pi^2}{2mL_B^2} (n^2 - m^2)} \Rightarrow L_A = L_B \sqrt{\frac{T_c}{T_h}}. \end{aligned} \quad (30)$$

For the cycle to be consistent with the second law, it must satisfy the condition in Eq. (6), i.e,

$$\begin{aligned} \frac{Q_{\text{hot}}}{T_h} + \frac{Q_{\text{cold}}}{T_c} &= S_B - S_A + \sum_n \frac{E_n^B}{T_c} (p_n^C - p_n^B), \\ &= S_B - S_C + \sum_n \frac{E_n^B}{T_c} (p_n^C - p_n^B), \quad (\text{using Eq.(28)}), \\ &= \sum_n p_n^B \left[-k_B \ln p_n^B - \frac{E_n^B}{T_c} \right] + \sum_n p_n^C \left[k_B \ln p_n^C + \frac{E_n^B}{T_c} \right], \end{aligned} \quad (31)$$

$$\text{From Eq.(22), we have, } \quad p_n^B = \frac{e^{-\beta_h E_n^B}}{Z_B}, \quad p_n^C = \frac{e^{-\beta_c E_n^C}}{Z_C}. \quad (32)$$

Rearranging Eq.(31) and using Eq.(32) gives,

$$\begin{aligned} \frac{Q_{\text{hot}}}{T_h} + \frac{Q_{\text{cold}}}{T_c} &= \sum_n p_n^B \left[-k_B \ln \frac{e^{-\beta_h E_n^B}}{Z_B} - \frac{E_n^B}{T_c} \right] \\ &\quad + \sum_n p_n^C \left[k_B \ln \frac{e^{-\beta_c E_n^C}}{Z_C} + \frac{E_n^B}{T_c} \right], \\ &= \sum_n p_n^B \left[\frac{E_n^B}{T_h} - \frac{E_n^B}{T_c} + k_B \ln (Z_B) \right] \\ &\quad + \sum_n p_n^C \left[-\frac{E_n^C}{T_c} + \frac{E_n^B}{T_c} - k_B \ln (Z_C) \right], \end{aligned}$$

from Eq. (26), and as $\sum_n p_n^B = \sum_n p_n^C = 1$, the above result reduces to,

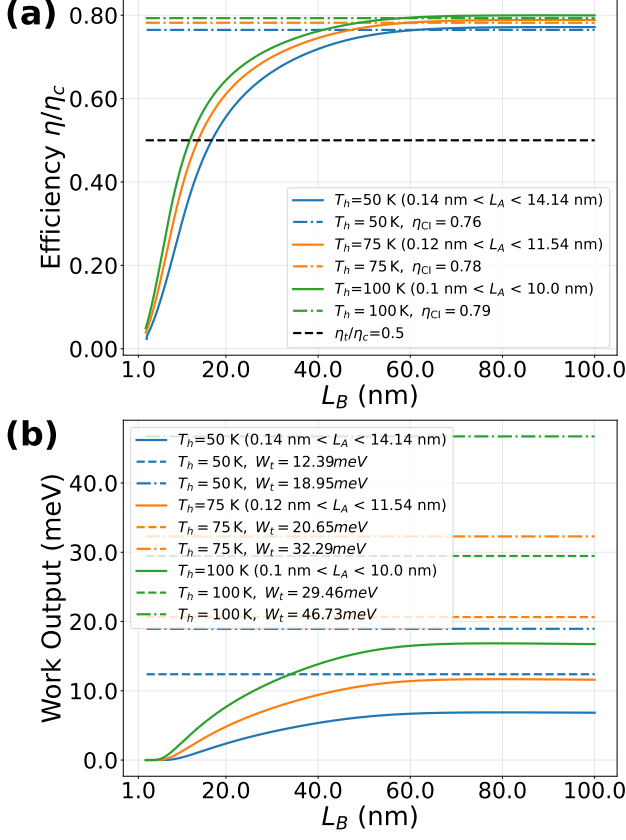


FIG. 4: (a) Efficiency in units of η/η_c and (b) Work output (in meV) for a particle in an IPW undergoing a three-stroke quantum isochoric cycle working as a heat engine at different hot bath temperatures. In (a), the black dashed line corresponds to η_{CT}/η_c from Eq. (13) (classical triangular cycle), while the dotted-dashed line shows η_{CI}/η_c from Eq. (20) (classical isochoric cycle). In (b), the dashed and dotted-dashed lines indicate the work outputs W_{CT} (Eq. (10)) and W_{CI} (Eq. (17)) for a monoatomic ideal gas undergoing the classical triangular and classical isochoric cycles, respectively. L_B is the length of the well during the quantum isochoric process and $T_c = 1\text{K}$.

$$\begin{aligned}
\frac{Q_{\text{hot}}}{T_h} + \frac{Q_{\text{cold}}}{T_c} &= k_B[\ln Z_B - \ln Z_C] + \left(\frac{1}{T_h} - \frac{1}{T_c}\right) \sum_n p_n^B E_n^B, \\
&= -k_B \left[\ln \left(\frac{Z_C}{Z_B} \right) + (\beta_c - \beta_h) \sum_n p_n^B E_n^B \right], \\
&= -k_B \left[\sum_n p_n^B \left(\ln \left(\frac{Z_C}{Z_B} \right) + \ln(e^{(\beta_c - \beta_h)} E_n^B) \right) \right], \\
&= -k_B \sum_n p_n^B \ln \left(\frac{e^{(\beta_c - \beta_h)} E_n^B}{Z_B/Z_C} \right) = -k_B \sum_n p_n^B \ln \left(\frac{\frac{e^{-\beta_h} E_n^B}{Z_B}}{\frac{e^{-\beta_c} E_n^B}{Z_C}} \right) \\
&= -k_B \sum_n p_n^B \ln \left(\frac{p_n^B}{p_n^C} \right) = -k_B \mathcal{D}(p^B \| p^C) \leq 0. \quad (33)
\end{aligned}$$

p_n^i, E_n^i, S_i, Z_i , and U_i denote the thermal probabilities, energy levels, entropy, partition function, and internal energy at point $i \in \{A = (L_A, T_h), B = (L_B, T_h), C = (L_B, T_c)\}$ in parameter space, in Fig.3. Finally, $\mathcal{D}(p \| q) = \sum_n p_n \ln \left(\frac{p_n}{q_n} \right)$ is the Kullback–Leibler relative entropy between two probability distributions p and q , which is always non-negative [22, 31]. Since Eq. (6) is satisfied, the cycle is thermodynamically feasible. For one complete cycle, the entropy change for bath and system can be found using Eqs. (5) and (33),

$$\Delta S_{\text{sys}} = 0, \quad \Delta S_{\text{tot}} = \Delta S_{\text{bath}} = k_B \mathcal{D}(p^B \| p^C) \geq 0. \quad (34)$$

For the three-stroke quantum isochoric cycle operating as a heat engine, the total work done by the system per cycle is given by $W = Q_{\text{hot}} + Q_{\text{cold}}$, where the heat exchanged Q_{hot} and Q_{cold} are defined in Eqs. (25) and (27). The work done, efficiency and coefficient of merit are then given as,

$$\begin{aligned}
W &= T_h [S_B(L_B, T_h) - S_A(L_A, T_h)] \\
&\quad - \sum_n E_n(L_B) [p_n^B(L_B, T_h) - p_n^C(L_B, T_c)], \quad \text{and} \\
\eta &= \frac{W}{Q_{\text{hot}}} = 1 - \frac{\sum_n E_n(L_B) [p_n^B(L_B, T_h) - p_n^C(L_B, T_c)]}{T_h [S_B(L_B, T_h) - S_A(L_A, T_h)]}, \\
\text{with, } \text{Coefficient of Merit} &= W \times \frac{\eta}{\eta_c}. \quad (35)
\end{aligned}$$

Fig. 4(a) and (b) show the efficiency and work output, respectively, for a particle confined in an IPW operating as a three-stroke quantum isochoric heat engine. Both efficiency and work output increase with the temperature difference between the baths and tend to saturate for large well length L_B . The efficiency of the quantum isochoric cycle exceeds that of the classical triangular cycle and saturates at larger L_B slightly above the efficiency of a classical three-stroke isochoric cycle. In the limit $T_h \rightarrow \infty$, Eq. (13) gives $\eta_{CT} = \eta_c/2$ for the triangular cycle, while from Eqs. (20) and (35) the efficiency of the classical and quantum isochoric cycle approaches the classical four-stroke Carnot efficiency. The work done by a particle in an IPW undergoing the quantum isochoric cycle does not exceed the work produced by a monoatomic ideal gas operating in the classical triangular and classical isochoric cycles between the same temperatures.

D. Three-Stroke Quantum Isoenergetic Cycle for Quantum Particle in an Infinite Potential well

This cycle was first, studied in Ref. [20], and considers a particle in a 1D IPW of variable length L that interacts

with a single heat bath at temperature T_h . The cycle (Figs. 1 (purple line) and 5) consists of three strokes, an isothermal stroke ($A \rightarrow B$), an isoenergetic stroke where the internal energy is held constant ($B \xrightarrow{\text{Purple}} C$), and an adiabatic stroke ($C \rightarrow A$). The exact derivation for the heat exchanged and the work performed can be found in Ref. [20]. Here, we briefly review the cycle.

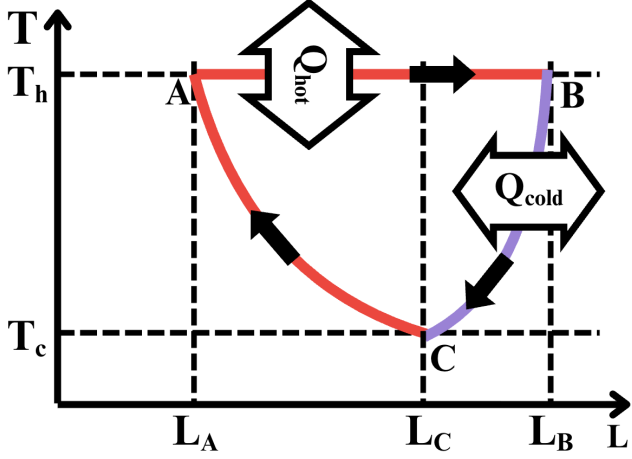


FIG. 5: Length - Temperature diagram of the IPW for a three-stroke quantum isoenergetic cycle. Stroke $A \rightarrow B$ is the isothermal stroke, $B \xrightarrow{\text{Purple}} C$ is the isoenergetic stroke, and $C \rightarrow A$ is the adiabatic stroke.

- **Stroke $A \rightarrow B$ (Isothermal):** The system, initially coupled to the hot bath at temperature T_h with well length L_A , undergoes an expansion. The well length changes from L_A to L_B at constant temperature T_h . The heat absorbed from the hot bath is given by,

$$Q_{\text{hot}} = T_h [S_B(L_B, T_h) - S_A(L_A, T_h)]. \quad (36)$$

- **Stroke $B \xrightarrow{\text{Purple}} C$ (Isoenergetic):** This stroke is performed at constant internal energy, and the system is brought to an effective temperature T_c while the well length changes to L_C . This step imposes the condition,

$$U_B(L_B, T_h) = U_C(L_C, T_c), \quad (37)$$

the heat rejected (Q_{cold}) during this process is equal to the work exchanged (W') [20],

$$Q_{\text{cold}} = W' = \int_{L_B}^{L_C} f(L, T) dL, \quad (38)$$

where $f(L, T) = -\sum_n \frac{\partial E_n(L)}{\partial L} p_n(L, T)$, is the generalized force. For a particle in an IPW, $\frac{\partial E_n(L)}{\partial L} = -2 \frac{E_n(L)}{L}$, which implies $f(L, T) = 2 \frac{U(L, T)}{L}$ (see Eq.(5) in Ref.[20]). Since,

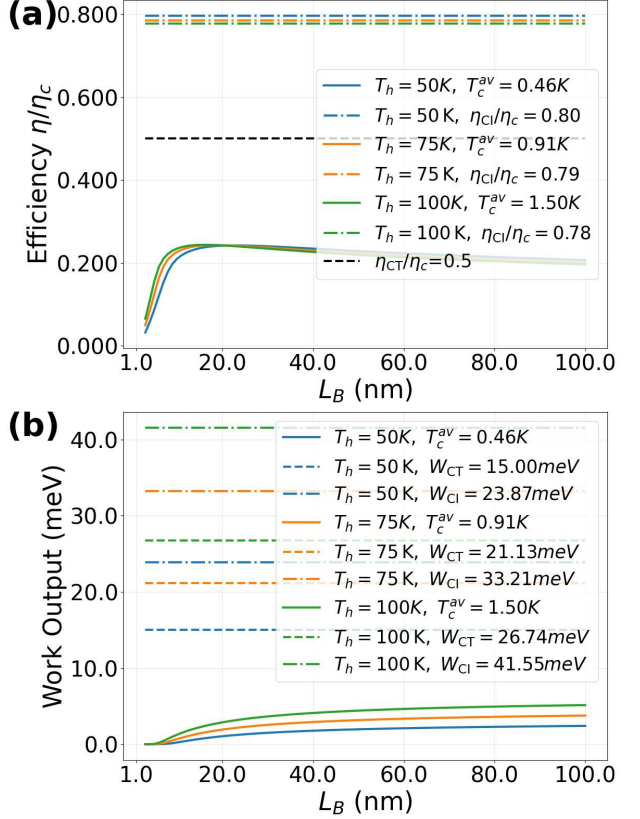


FIG. 6: (a) Efficiency in units of η/η_c and (b) Work output (in meV) for a particle in an IPW undergoing a three-stroke quantum isoenergetic cycle working as a heat engine at different bath temperatures. In (a), the black dashed line corresponds to η_{CT}/η_c from Eq. (13) (classical triangular cycle), while the dotted-dashed line shows η_{CI}/η_c from Eq. (20) (classical isochoric cycle). In (b), the dashed and dotted-dashed lines indicate the work outputs W_{CT} (Eq. (10)) and W_{CI} (Eq. (17)) for a monoatomic ideal gas undergoing the classical triangular and classical isochoric cycles, respectively. Cold bath temperature used for the classical triangular and classical isochoric cycle is taken to be the average of T_c attained by the system at the end of the isoenergetic stroke within the length considered. L_B is the initial length of the well during the isoenergetic process and $L_A = 1\text{nm}$.

internal energy is kept constant throughout this stroke, we obtain,

$$Q_{\text{cold}} = -2U_B(L_B, T_h) \ln\left(\frac{L_B}{L_C}\right). \quad (39)$$

- **Stroke $C \rightarrow A$ (Adiabatic):** The system returns to its initial state without heat exchange in this stroke, which obeys the adiabatic condition;

$$S_A(L_A, T_h) = S_C(L_C, T_c), \quad (40)$$

which, following a derivation similar to Eq.(30), reduces

to, (see, Eq.(12) of Ref.[20])

$$L_C = L_A \sqrt{\frac{T_h}{T_c}}. \quad (41)$$

The two conditions, Eqs. (37) and (41), are solved simultaneously to determine L_C and T_c numerically. It should be emphasized that T_c is not the bath temperature but rather the effective temperature, the system reaches at the end of the isoenergetic process, and it depends on the parameters: L_A, L_B and T_h . The total work performed $W = Q_{\text{hot}} + Q_{\text{cold}}$, is obtained from Eqs.(36) and (39), and the efficiency of the cycle is given by,

$$\eta = \frac{W}{Q_{\text{hot}}} = 1 - \frac{2U_B(L_B, T_h)}{Q_{\text{hot}}} \ln\left(\frac{L_B}{L_C}\right). \quad (42)$$

Fig. 6(a) and (b) present the corresponding efficiency and work output for a particle in an IPW under a three-stroke quantum isoenergetic cycle. In this cycle, both efficiency and work output exhibit only mild dependence on the bath temperature T_h , with work output showing a slight increase as T_h grows. We compare the quantum isoenergetic cycle's performance with a classical triangular and classical isochoric cycle operating between T_h and T_c^{av} , where T_c^{av} is the average effective cold temperature for a particle in an IPW undergoing the three-stroke quantum isoenergetic cycle across the considered L_B range. In this comparison, we observe that both the efficiency and the work output of the quantum isoenergetic cycle remain below those of the classical triangular and classical isochoric cycle.

Unlike the single-bath isoenergetic cycle, where increasing T_h does not enhance efficiency (see, Fig.6(a)), the three-stroke quantum isochoric cycle in Sec.IIB, demonstrates clear gains in both efficiency and work output (see, Fig.4(a) and (b)). A performance comparison between the three-stroke quantum isochoric and isoenergetic cycles is presented in Table I. The temperature of the cold bath during the quantum isochoric cycle, T_c , is fixed at 1 K. This T_c is approximately the effective cold temperature achieved in the isoenergetic cycle for the parameters considered. The results indicate that the quantum isochoric cycle achieves superior efficiency, work output and a higher overall coefficient of merit compared to isoenergetic cycle. Furthermore, implementing a quantum isochoric stroke is experimentally more feasible than realizing a quantum isoenergetic stroke [32, 33]. For these reasons, in the following section we concentrate on graphene-based systems undergoing the quantum isochoric cycle.

III. LANDAU LEVELS OF GRAPHENE SYSTEMS

In the presence of a perpendicular magnetic field, for MLG and BLG, the Landau level energies $E_n^{\text{MLG}}(B)$ and

$E_n^{\text{BLG}}(B)$ are calculated using the low-energy effective Hamiltonians near the Dirac points [34–37], i.e,

$$E_n^{\text{MLG}}(B) = \pm v_f \sqrt{2eB\hbar n}, \quad E_n^{\text{BLG}}(B) = \pm \frac{\hbar eB}{m_{\text{eff}}} \sqrt{n(n-1)} \quad (43)$$

where $m_{\text{eff}} \approx 0.035m_e$ the effective electron mass in BLG [37]. For TBG, the continuum model consists of two Dirac-like Hamiltonians for each layer, coupled via interlayer tunneling across the rotated layers [35, 38]. Restricting interactions to the first moiré shell yields an effective eight-band Hamiltonian [38–40],

$$\mathcal{H}_{\theta}^{\text{TBG}}(\mathbf{k}) = \begin{bmatrix} h_{\theta/2}^{\text{MLG}}(\mathbf{k}) & T_b & T_{tr} & T_{tl} \\ T_b^{\dagger} & h_{-\theta/2}^{\text{MLG}}(\mathbf{k}_b) & 0 & 0 \\ T_{tr}^{\dagger} & 0 & h_{-\theta/2}^{\text{MLG}}(\mathbf{k}_{tr}) & 0 \\ T_{tl}^{\dagger} & 0 & 0 & h_{-\theta/2}^{\text{MLG}}(\mathbf{k}_{tl}) \end{bmatrix} \quad (44)$$

where \mathbf{k} is the momentum in the moiré Brillouin zone, and $\mathbf{k}_i = \mathbf{k} + \tilde{\mathbf{k}}_i$ with $i \in \{\text{b, tr, tl}\}$ indexing the shifted momenta $\tilde{\mathbf{k}}_i$. $h_{\theta}^{\text{MLG}}(\mathbf{k})$ denotes the monolayer Dirac Hamiltonian rotated by θ [23, 35, 41]. The shifted momenta are given as,

$$\tilde{\mathbf{k}}_b = \kappa_{\theta}(0, -1), \quad \tilde{\mathbf{k}}_{tr} = \kappa_{\theta}\left(\frac{\sqrt{3}}{2}, \frac{1}{2}\right), \quad \tilde{\mathbf{k}}_{tl} = \kappa_{\theta}\left(-\frac{\sqrt{3}}{2}, \frac{1}{2}\right), \quad (45)$$

with $\kappa_{\theta} = \frac{8\pi}{3a} \sin(\theta/2)$, where $a = 2.46\text{\AA}$ is the graphene lattice constant. The interlayer hopping matrices are given as,

$$T_b = \omega \begin{bmatrix} 1 & 1 \\ 1 & 1 \end{bmatrix}, \quad T_{tr} = \omega \begin{bmatrix} e^{-i\phi} & 1 \\ e^{i\phi} & e^{-i\phi} \end{bmatrix}, \quad T_{tl} = \omega \begin{bmatrix} e^{i\phi} & 1 \\ e^{-i\phi} & e^{i\phi} \end{bmatrix}, \quad (46)$$

with $\omega = 110$ meV being the interlayer hopping energy and $\phi = 2\pi/3$ [38]. This Hamiltonian can be reduced to a two-band model [35, 38],

$$\mathcal{H}_{\theta}^{\text{TBG}}(\mathbf{k} \approx \mathbf{0}) = \hbar v_f^* \sigma^* \cdot \mathbf{k}, \quad v_f^* = v_f \frac{1 - 3\alpha_{\theta}^2}{1 + 6\alpha_{\theta}^2}, \quad (47)$$

with v_f^* representing the renormalized Fermi velocity and $\alpha_{\theta} = \omega/(\hbar v_f \kappa_{\theta})$ defining the dimensionless interlayer coupling. The renormalized Fermi velocity v_f^* goes to zero at the magic angle $\theta^* = 1.05^\circ$, which indicates the presence of a flat band dispersion. The complete derivation of Landau levels for TBG in a magnetic field is provided in Ref. [35].

A. Three-Stroke Quantum Isochoric Cycle for Graphene Based system

Similar to a quantum particle in an IPW, a three-stroke quantum isochoric cycle can be defined for graphene based

Parameters and Performance Metric	$L_B = 50.0 \text{ nm}$		$L_B = 100.0 \text{ nm}$	
	Three-Stroke Quantum Isochoric Cycle	Three-Stroke Quantum Isoenergetic Cycle	Three-Stroke Quantum Isochoric Cycle	Three-Stroke Quantum Isoenergetic Cycle
Length L_A in nm	5.270	1.0	10.541	1.0
Cold temperature T_c in K	1.0	1.006	1.0	0.965
Efficiency (η/η_c)	0.779	0.220	0.796	0.197
Work done (W) in meV	13.610	3.905	14.642	4.579
Coefficient of Merit $(W \times \eta/\eta_c)$ in meV	10.602	0.859	11.649	0.904

TABLE I: Performance comparison of particle in a 1D IPW undergoing a three-stroke quantum isochoric cycle versus that of one undergoing a three-stroke quantum isoenergetic cycle for different L_B values with hot bath temperature $T_h = 90 \text{ K}$. The cold bath temperature for the three-stroke quantum isochoric cycle is $T_c = 1.0 \text{ K}$, the length L_C for three-stroke isoenergetic cycle for the parameters $L_B = 50.0 \text{ nm}$ and $L_B = 100.0 \text{ nm}$ are $L_C = 9.45 \text{ nm}$ and $L_C = 9.65 \text{ nm}$ respectively. The bolded numbers highlight the three-stroke cycle with superior performance metric for the given parameters considered.

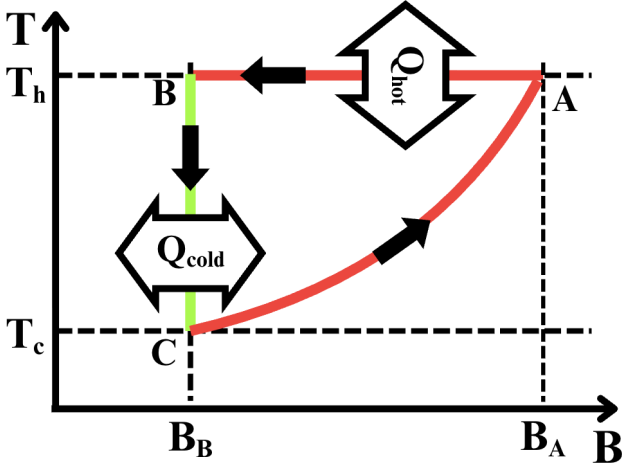


FIG. 7: Magnetic field - Temperature (B-T) diagram for graphene based systems in a three-stroke quantum isochoric cycle. Stroke $A \rightarrow B$ is the isothermal stroke, $B \xrightarrow{\text{Green}} C$ is the quantum isochoric stroke, and $C \rightarrow A$ is the adiabatic stroke.

systems, with the magnetic field B replacing the well length as the tunable parameter. The Landau level energies for graphene based systems can be obtained using Eqs.(43) and (44). We can then define thermal state $(\rho(B, T))$ for a graphene based systems as, [4, 14, 15],

$$\rho(B, T) = \sum_n p_n |n\rangle \langle n|, \quad \text{with} \quad p_n(B, T) = \frac{e^{-\beta E_n(B)}}{Z}, \quad (48)$$

and $Z(B, T) = \sum_n e^{-\beta E_n(B)},$

where $p_n(B, T)$ are the occupation probabilities, $Z(B, T)$ is the partition function and $\beta = \frac{1}{k_B T}$, where k_B is the Boltzmann constant. Once the thermal state is determined, other thermodynamic quantities can be computed, such

as entropy $S = -k_B \sum_n p_n \ln p_n$ and internal energy $U = \sum_n p_n E_n$. For infinitesimal transformations, using Eq. (1), we obtain for the work done and heat exchanged,

$$W = - \sum_n p_n(B, T) dE_n, \quad Q = \sum_n E_n(B) dp_n. \quad (49)$$

These relations are used to evaluate the performance of various graphene based systems. Now, we briefly discuss the three stroke quantum isochoric cycle for graphene based systems as depicted in Fig.7.

- **Stroke $A \rightarrow B$ (Isothermal):** The system in equilibrium with the hot bath at temperature T_h at magnetic field B_A is brought to a magnetic field B_B isothermally. The heat absorbed from the hot reservoir can be calculated using Eq.(49),

$$Q_{\text{hot}} = \sum_n \int_{B_A}^{B_B} E_n(B) \frac{\partial p_n(B, T)}{\partial B} dB, \quad (50)$$

which reduces to (see Appendix A),

$$Q_{\text{hot}} = T_h (S_B(B_B, T_h) - S_A(B_A, T_h)). \quad (51)$$

- **Stroke $B \xrightarrow{\text{Green}} C$ (Isochoric):** The magnetic field is held constant at B_B as the system thermalizes to temperature T_c of the cold bath. The heat rejected to the cold reservoir is obtained using Eq.(49),

$$Q_{\text{cold}} = \sum_n E_n(B_B) (p_n^C(B_B, T_c) - p_n^B(B_B, T_h)). \quad (52)$$

- **Stroke $C \rightarrow A$ (Adiabatic):** The system is decoupled from the bath and the magnetic field is changed back to its initial value B_A with no heat exchange. As this is an isoentropic process, we have,

$$S_C(B_B, T_c) = S_A(B_A, T_h). \quad (53)$$

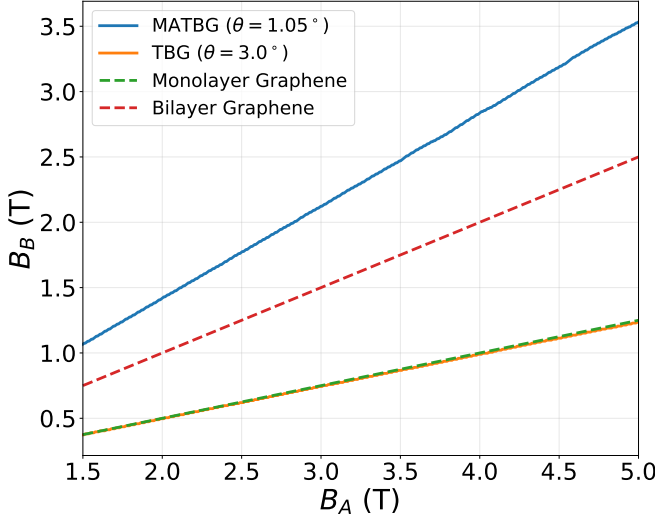


FIG. 8: Adiabatic condition from Eq. (53) relating the initial and final magnetic fields B_A and B_B for graphene-based systems, with bath temperatures $T_h = 100\text{K}$ and $T_c = 50\text{K}$.

Systems	α
MLG	$2.0000 \pm 0.0000 \approx 2.0$
BLG	$1.0000 \pm 0.0000 \approx 1.0$
MATBG ($\theta = 1.05^\circ$)	$0.4977 \pm 0.0001 \approx 0.5$
TBG ($\theta = 3.0^\circ$)	$2.0140 \pm 0.0002 \approx 2.0$

TABLE II: Best-fit values of the exponent α in the relation $B_B = B_A(T_c/T_h)^\alpha$ for different graphene-based systems at $T_h = 100\text{K}$ and $T_c = 50\text{K}$.

As shown earlier in Sec. II C, Eqs.(33) and (34), the second law of thermodynamics holds for three-stroke quantum isochoric cycle. Since this derivation is general, it also applies to this cycle, yielding the same entropy changes as in Eq. (34). The net work done can be obtained from Eqs. (51) and (52) as $W = Q_{\text{cold}} + Q_{\text{hot}}$. The work done and efficiency is then,

$$W = T_h (S_B(B_B, T_h) - S_A(B_A, T_h)) - \sum_n E_n(B_B) (p_n^B(B_B, T_h) - p_n^C(B_B, T_c)), \quad (54)$$

$$\eta = 1 - \frac{\sum_n E_n(B_B) (p_n^B(B_B, T_h) - p_n^C(B_B, T_c))}{T_h (S_B(B_B, T_h) - S_A(B_A, T_h))}.$$

For MLG and BLG, the adiabatic condition imposes stricter constraints on the thermal probabilities due to the energy-scaling condition [14, 23, 29],

$$p_n^C(B_B, T_c) = p_n^A(B_A, T_h) \quad \forall n. \quad (55)$$

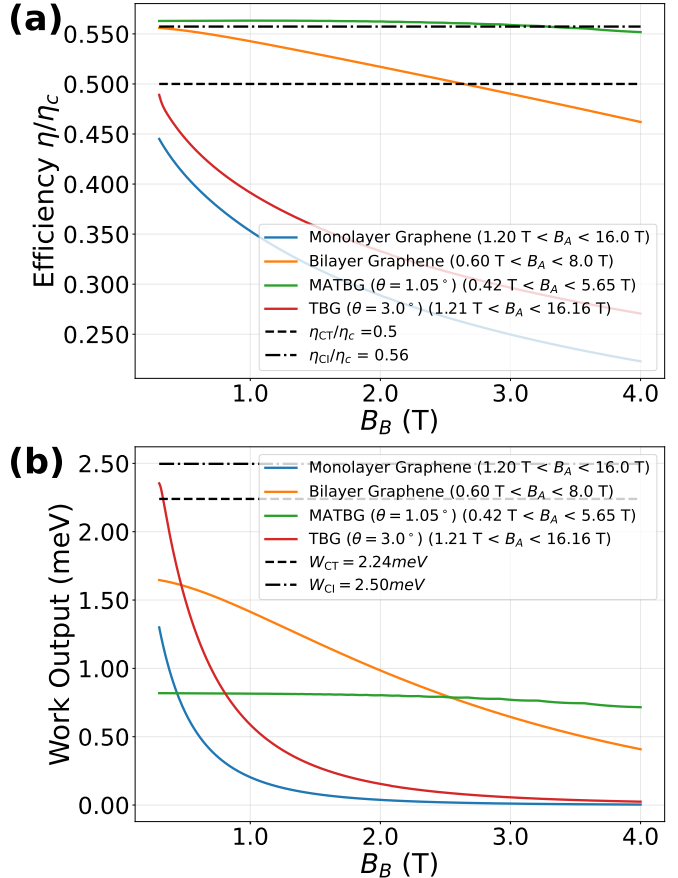


FIG. 9: (a) Efficiency in units of η/η_c and (b) Work output (in meV) for graphene based systems undergoing a three-stroke quantum isochoric cycle. B_B is the external magnetic field during the quantum isochoric process. In (a), the black dashed line corresponds to η_{CT}/η_c from Eq. (13) (classical triangular cycle), while the dotted-dashed line shows η_{CI}/η_c from Eq. (20) (classical isochoric cycle). In (b), the dashed and dotted-dashed lines indicate the work outputs W_{CT} (Eq. (10)) and W_{CI} (Eq. (17)) for a monoatomic ideal gas undergoing the classical triangular and classical isochoric cycles, respectively, at $T_h = 100\text{K}$ and $T_c = 50\text{K}$.

Following an analogous derivation to that of Eq. (41), we obtain explicit scaling relations linking the magnetic field to the bath temperatures,

$$B_B = B_A \left(\frac{T_c}{T_h} \right)^2 \quad (\text{MLG}), \quad B_B = B_A \left(\frac{T_c}{T_h} \right) \quad (\text{BLG}). \quad (56)$$

Since an analytical expression for the Landau levels of TBG cannot be obtained, we determine the relation between B_B and B_A using Eq. (53). Fig. 8 illustrates this relation across different graphene systems. We observe that the isoentropic lines of TBG at larger twist angles (i.e., $\theta \approx 3^\circ$) coincide with those of MLG, reflecting the effective decoupling of TBG into MLG at large angle regime, as predicted

Systems	Parameters		Efficiency (η/η_c)
	B_A in T or L_A in nm	B_B in T or L_B in nm	
MLG	$B_A = 1.756$	$B_B = 0.439$	0.418
BLG	$B_A = 4.916$	$B_B = 2.458$	0.505
MATBG ($\theta = 1.05^\circ$)	$B_A = 1.392$	$B_B = 0.986$	0.563
TBG ($\theta = 3.0^\circ$)	$B_A = 3.268$	$B_B = 0.809$	0.408
Particle in a 1D IPW	$L_A = 6.547$	$L_B = 9.259$	0.536

TABLE III: Efficiency in units of η/η_c and parameters for graphene based systems and particle in an IPW under the three-stroke quantum isochoric cycle at identical work output $W = 0.815$ meV for all systems. η_c is the Carnot efficiency, and the bath temperatures are $T_h = 100$ K and $T_c = 50$ K. The bolded number highlight the system with highest efficiency at equal work output, for the parameters considered.

in Refs.[35, 39]. Using a linear fit to the data in Fig. 8, we find the coefficient α for the relation $B_B = B_A(T_c/T_h)^\alpha$. Table II lists the obtained values for the different graphene-based systems for $T_h = 100$ K and $T_c = 50$ K.

IV. RESULTS AND DISCUSSION

In this section, we present numerical results for graphene based systems operating under a three-stroke quantum isochoric cycle. For computational accuracy, we take the first 500 Landau levels, which has been verified to yield convergent and reliable results across various graphene systems [23, 35, 41]. All numerical codes used to produce the results and figures in this work are available in [42].

Fig. 9 (a) and (b) illustrate the performance of various graphene platforms operating under the three-stroke quantum isochoric cycle. We see that the thermodynamic efficiency of MATBG surpasses that of other graphene platforms, and it exceeds the classical triangular cycle efficiency across the entire range of the magnetic field and slightly surpasses the three-stroke classical isochoric cycle efficiency for lower magnetic field B_B considered. Large-angle TBG and MLG display the lowest efficiency and work output, both of which decrease rapidly as B_B increases. BLG on the other hand is seen to operate with modest efficiency and work output, with the efficiency dropping below the classical triangular cycle efficiency for larger values of B_B . From Fig. 8 and Table II, it is evident that the magnetic field values B_B and B_A are relatively closer for MATBG than for other graphene based systems operating between bath temperatures $T_h = 100$ K and $T_c = 50$ K. This results in a smaller work output for MATBG, as the area enclosed by the quantum three-stroke isochoric cycle will be smaller.

Nevertheless, MATBG achieves higher efficiency, indicating a more effective conversion of input heat into work (see, Fig. 9). Since the cycle sizes differ across graphene based systems, we compare their efficiencies at equivalent work output for a fair performance assessment. Table III provides an analysis of efficiency and the required parameters for equal work output in graphene based systems and a particle in an IPW, operating under a three-stroke quantum isochoric cycle with bath temperatures $T_c = 50$ K and $T_h = 100$ K. This reveals that MATBG attains the highest efficiency at similar work output despite operating within a smaller cycle in the parameter space. The smaller area of the three-stroke quantum isochoric cycle of MATBG due to relatively close B_B and B_A , leads to reduced heat absorption from the hot bath, as depicted in Eq. (51) in turn due to a smaller entropy difference. However, MATBG rejects even less heat to the cold bath, as per Eq. (52), owing to smaller Landau level energies and spacing (see, Appendix B). These factors collectively enable MATBG to achieve higher efficiency with moderate work output.

V. EXPERIMENTAL REALIZATION AND CONCLUSION

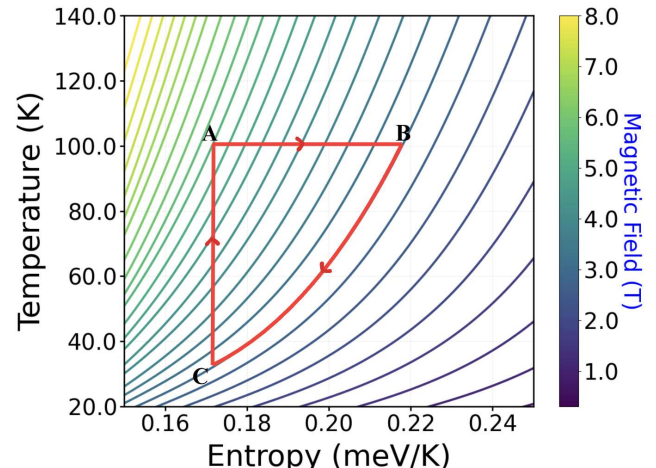


FIG. 10: T-S diagram of MATBG with isochoric contour lines

Figure 10 shows the temperature–entropy (T–S) diagram for MATBG, highlighting the isochoric contours and the three-stroke quantum isochoric cycle explored in this work. Realizing such a cycle experimentally requires precise control of both temperature and magnetic field, with feasibility determined by the ability to implement each thermodynamic stroke reliably. A quantum isochoric stroke can be achieved by coupling the system to a thermal reservoir while maintaining a constant magnetic field, an operation that is considerably more accessible experimentally than the quantum isoenergetic stroke [32, 33]. Few-stroke

engines further reduce experimental overhead by minimizing the number of required control operations per cycle while retaining quantum-enhanced performance [11]. Recent advances in nanoscale thermodynamic measurements, such as single-electron transistor, based thermometry and scanning thermoelectric probes capable of entropy mapping [43–45], provide the essential tools for implementing and characterizing quantum thermodynamic cycles in MATBG and other strongly correlated two-dimensional materials.

In this work, we introduced and analyzed a three-stroke quantum isochoric cycle operating as a heat engine between two thermal reservoirs. Using a particle in a one-dimensional infinite potential well as a prototype system, we demonstrated that the cycle achieves higher efficiency than the classical triangular engine, which reaches only half the Carnot limit, and also surpasses the performance of the previously proposed three-stroke quantum isoenergetic cycle [20]. We then extended our analysis to graphene-based systems under perpendicular magnetic fields, including monolayer graphene (MLG), AB-stacked bilayer graphene (BLG), and twisted bilayer graphene (TBG) at both magic and non-magic angles. Among these platforms,

magic-angle TBG (MATBG) achieves the highest efficiency for comparable work output, even with a smaller cycle size. This result underscores the promise of engineered quantum materials, particularly those with tunable flat-band electronic structures such as TBG, as optimal working substances for controllable, high-performance quantum thermodynamic devices.

Overall, the three-stroke quantum isochoric cycle offers distinct experimental advantages for probing and exploiting thermodynamic behavior in complex quantum materials. Its reduced operational complexity makes it well suited for nanoscale implementations, while its ability to leverage quantum effects provides a pathway toward enhanced thermodynamic performance. When combined with state-of-the-art experimental techniques, such as nanoscale thermometry, entropy imaging, and magneto-transport measurements [46], the cycle provides a powerful framework for studying microscopic energy-conversion mechanisms in quantum systems. More broadly, our results position tunable moiré materials and low-dimensional heterostructures as versatile platforms for developing functional quantum thermodynamic technologies, including efficient nanoscale energy harvesters and integrated quantum cooling architectures.

-
- [1] R. Uzdin, A. Levy, and R. Kosloff. Equivalence of quantum heat machines, and quantum-thermodynamic signatures. *Physical Review X*, 5(3):031044, (2015).
- [2] R. Kosloff. Quantum thermodynamics: A dynamical viewpoint. *Entropy*, 15(6):2100–2128, (2013).
- [3] S. Bhattacharjee and A. Dutta. Quantum thermal machines and batteries. *The European Physical Journal B*, 94(12):239, (2021).
- [4] S. Vinjanampathy and J. Anders. Quantum thermodynamics. *Contemporary Physics*, 57(4):545–579, (2016).
- [5] J. Millen and A. Xuereb. Perspective on quantum thermodynamics. *New Journal of Physics*, 18(1):011002, (2016).
- [6] J. B. Brask, G. Haack, N. Brunner, and M. Huber. Autonomous quantum thermal machine for generating steady-state entanglement. *New Journal of Physics*, 17(11):113029, (2015).
- [7] N. M. Myers, O. Abah, and S. Deffner. Quantum thermodynamic devices: From theoretical proposals to experimental reality. *AVS quantum science*, 4(2), (2022).
- [8] J. P. Peterson, T. B. Batalhão, R. Sampaio, A. M. Souza, R. M. Serra, and I. S. Oliveira. Experimental demonstration of a quantum heat engine with a single trapped ion. *Physical Review Letters*, 123(24):240601, (2019).
- [9] J. Roßnagel, S. T Dawkins, K. N Tolazzi, O. Abah, E. Lutz, F. Schmidt-Kaler, and K. Singer. A single-atom heat engine. *Science*, 352(6283):325–329, (2016).
- [10] T. Uusnäkki, T. Mörstedt, W. Teixeira, M. Rasola, and M. Möttönen. Experimental realization of a quantum heat engine based on dissipation-engineered superconducting circuits. *arXiv preprint*, 2502:20143, (2025).
- [11] J. Klatzow, J. N. Becker, P. M. Ledingham, C. Weinzel, K. T. Kaczmarek, D. J. Saunders, J. Nunn, I. A. Walmsley, R. Uzdin, and E. Poem. Experimental demonstration of quantum effects in the operation of microscopic heat engines. *Physical Review Letters*, 122(11):110601, (2019).
- [12] Q. Bouton, J. Nettersheim, S. Burgardt, D. Adam, E. Lutz, and A. Widera. A quantum heat engine driven by atomic collisions. *Nature Communications*, 12:2063, (2021).
- [13] Yan-Lei Zhang, Z. Shen, Chun-Hua Dong, Chang-Ling Zou, and Guang-Can Guo. Optomechanical quantum heat engine with coupled photonic and phononic modes. *Physical Review Letters*, 125(7):073604, (2020).
- [14] H. T. Quan, Yu-xi Liu, Chang-Pu Sun, and F. Nori. Quantum thermodynamic cycles and quantum heat engines. *Physical Review E—Statistical, Nonlinear, and Soft Matter Physics*, 76(3):031105, (2007).
- [15] H. T. Quan. Quantum thermodynamic cycles and quantum heat engines. ii. *Physical Review E—Statistical, Nonlinear, and Soft Matter Physics*, 79(4):041129, (2009).
- [16] S. Deffner and S. Campbell. *Quantum Thermodynamics: An Introduction*. IOP Concise Physics. Morgan & Claypool Publishers, San Rafael, CA, (2019).
- [17] O. Abah and E. Lutz. Efficiency of heat engines coupled to nonequilibrium reservoirs. *Europhysics Letters*, 106(2):20001, (2014).
- [18] S. Koyanagi and Y. Tanimura. The laws of thermodynamics for quantum dissipative systems: A quasi-equilibrium helmholtz energy approach. *The Journal of Chemical Physics*,

- 157(1), (2022).
- [19] VF Lisboa, PR Dieguez, JR Guimarães, JFG Santos, and RM Serra. Experimental investigation of a quantum heat engine powered by generalized measurements. *Physical Review A*, 106(2):022436, (2022).
- [20] C. Ou and S. Abe. Exotic properties and optimal control of quantum heat engine. *Europhysics Letters*, 113(4):40009, (2016).
- [21] L. D. Landau and E. M. Lifshitz. *Statistical Physics: Volume 5*, volume 5. Elsevier, (2013).
- [22] G. T Landi and M. Paternostro. Irreversible entropy production: From classical to quantum. *Reviews of Modern Physics*, 93(3):035008, (2021).
- [23] H. M. Soufy and C. Benjamin. Enhanced performance across otto, carnot, and stirling cycles revealed by flat-band thermodynamics. *Physical Review A*, 112(5):052215, (2025).
- [24] B. Scharf, A. Braggio, E. Strambini, F. Giazotto, and E. M. Hankiewicz. Topological josephson heat engine. *Commun. Phys.*, 3(1):198, (2020).
- [25] Jochen Rau. *Statistical physics and thermodynamics: an introduction to key concepts*. Oxford University Press, (2017).
- [26] H. B Callen. *Thermodynamics & an introduction to thermosstatistics*. John wiley & sons, (2006).
- [27] L. D. Landau and E. M. Lifshitz. *Quantum mechanics: non-relativistic theory*, volume 3. Elsevier, (2013).
- [28] P. Adrien M. Dirac. *The principles of quantum mechanics*. Number 27. Oxford university press, (1981).
- [29] F. J Peña, O. Negrete, N. Cortés, and P. Vargas. Otto engine: Classical and quantum approach. *Entropy*, 22(7):755, (2020).
- [30] R. Dann and R. Kosloff. Quantum signatures in the quantum carnot cycle. *New Journal of Physics*, 22(1):013055, (2020).
- [31] R. M Gray. *Entropy and information theory*. Springer Science & Business Media, (2011).
- [32] F. J Peña, M. Ferré, PA Orellana, R. G Rojas, and P Vargas. Optimization of a relativistic quantum mechanical engine. *Physical Review E*, 94(2):022109, (2016).
- [33] T. Uusnäkki, T. Mörstedt, W. Teixeira, M. Rasola, and M. Möttönen. Experimental realization of a quantum heat engine based on dissipation-engineered superconducting circuits. *arXiv preprint arXiv:2502.20143*, (2025).
- [34] M. O. Goerbig. Electronic properties of graphene in a strong magnetic field. *Rev. Mod. Phys.*, 83(4):1193–1243, (2011).
- [35] J. Python. Quantum oscillations in twisted bilayer graphene. Master's thesis, Utrecht University, (2019).
- [36] E. McCann and M. Koshino. Electronic properties of monolayer and bilayer graphene. *Rep. Prog. Phys.*, 76(5):056503, (2013).
- [37] E. McCann and V. I. Fal'ko. Landau-level degeneracy and quantum hall effect in a graphite bilayer. *Phys. Rev. Lett.*, 96(8):086805, (2006).
- [38] R. Bistritzer and A. H. MacDonald. Moiré bands in twisted double-layer graphene. *Proc. Natl. Acad. Sci. U.S.A.*, 108(30):12233–12237, (2011).
- [39] R. Bistritzer and A. H. MacDonald. Moiré butterflies in twisted bilayer graphene. *Phys. Rev. B*, 84(3):035440, (2011).
- [40] J. M. B. Lopes dos Santos, N. M. R. Peres, and A. H. Castro Neto. Continuum model of the twisted graphene bilayer. *Phys. Rev. B*, 86(15):155449, (2012).
- [41] A. Singh and C. Benjamin. Magic angle twisted bilayer graphene as a highly efficient quantum otto engine. *Physical Review B*, 104(12):125445, (2021).
- [42] Codes used for obtaining operational phases and performance for graphene based systems under tunable external magnetic field for different thermodynamic cycles. <https://github.com/HadiMohammedSoufy/Three-Stroke-Thermodynamic-Cycles-in-Graphene-Heterostructure.git>.
- [43] A. Rozen, J. M. Park, U. Zondiner, Y. Cao, D. Rodan-Legrain, T. Taniguchi, K. Watanabe, Y. Oreg, A. Stern, E. Berg, et al. Entropic evidence for a pomeranchuk effect in magic-angle graphene. *Nature*, 592(7853):214–219, (2021).
- [44] A. Abualnaja, J. Zhu, J. Dai, Q. Tang, M. Zhu, and A. Luican-Mayer. Heavy fermions, mass renormalization, and local moments in magic-angle twisted bilayer graphene via planar tunneling spectroscopy. *arXiv preprint arXiv:2311.11818*, (2023).
- [45] A. Pyurbeeva, W. Zheng, Y. Zeng, P. Kurilovich, M. Zhu, and A. F. Young. Entropy thermometry of interacting electrons in magic-angle twisted bilayer graphene. *arXiv preprint arXiv:2112.09788*, (2021).
- [46] M. Mecklenburg, W. A Hubbard, ER White, R. Dhall, S. B Cronin, S. Aloni, and BC Regan. Nanoscale temperature mapping in operating microelectronic devices. *Science*, 347(6222):629–632, (2015).

Appendix A: Heat Exchange in Quantum Isothermal Processes

In quantum thermodynamics, an isothermal process is characterized by the system maintaining thermal equilibrium with a heat reservoir at a constant temperature as its external parameters change. For a quantum system subjected to a changing magnetic field B , this process ensures the system evolves through instantaneous thermal states. From the first law of thermodynamics, the infinitesimal heat exchange during such a process is given by the energy-level weighted change in occupation probabilities,

$$\delta Q = \sum_n E_n(B) dp_n(B, T), \quad (\text{A1})$$

where $E_n(B)$ are the energy eigenvalues and $p_n(B, T)$ are the occupation probabilities. For a finite change in magnetic field from B_1 to B_2 , the total heat exchanged becomes,

$$Q = \int_{B_1}^{B_2} \sum_n E_n(B) \frac{\partial p_n(B, T)}{\partial B} dB. \quad (\text{A2})$$

This integral is path-dependent in parameter space, reflecting the fact that heat is a path-dependent quantity. Now, consider the derivative of entropy ($S(B, T) = -k_B \sum_n p_n(B, T) \ln p_n(B, T)$) with respect to the magnetic field,

$$\begin{aligned} \frac{\partial S}{\partial B} &= -k_B \sum_n \left[\frac{\partial p_n}{\partial B} \ln p_n + p_n \frac{\partial}{\partial B} (\ln p_n) \right] \\ &= -k_B \sum_n \frac{\partial p_n}{\partial B} \ln p_n - k_B \sum_n \frac{\partial p_n}{\partial B}, \end{aligned} \quad (\text{A3})$$

where the second term vanishes due to probability conservation $\sum_n \partial p_n / \partial B = 0$. Thus,

$$\frac{\partial S}{\partial B} = -k_B \sum_n \frac{\partial p_n}{\partial B} \ln p_n(B, T). \quad (\text{A4})$$

Using the thermal distribution expression $\ln p_n(B, T) = -\beta E_n(B) - \ln Z(B, T)$, we substitute into Eq. (A4),

$$\begin{aligned} \frac{\partial S}{\partial B} &= -k_B \sum_n \frac{\partial p_n}{\partial B} (-\beta E_n - \ln Z) \\ &= \frac{1}{T} \sum_n \frac{\partial p_n}{\partial B} E_n + k_B \ln Z \sum_n \frac{\partial p_n}{\partial B}. \end{aligned} \quad (\text{A5})$$

The second term again vanishes due to probability conservation, yielding,

$$\frac{\partial S}{\partial B} = \frac{1}{T} \sum_n \frac{\partial p_n}{\partial B} E_n. \quad (\text{A6})$$

Integrating Eq. (A6) from B_1 to B_2 ,

$$\int_{B_1}^{B_2} \frac{\partial S}{\partial B} dB = \frac{1}{T} \int_{B_1}^{B_2} \sum_n \frac{\partial p_n}{\partial B} E_n dB. \quad (\text{A7})$$

Recognizing the right-hand side as Q/T from Eq. (A2), we obtain the fundamental isothermal relation,

$$S(B_2, T) - S(B_1, T) = \frac{Q}{T} \Rightarrow Q = T \Delta S, \quad (\text{A8})$$

where $\Delta S = S(B_2, T) - S(B_1, T)$. This result demonstrates that for quantum isothermal processes, the heat exchange is directly proportional to the entropy change, with the temperature serving as the proportionality constant. This relation holds regardless of the specific functional forms of $E_n(B)$.

Appendix B: Comparative analysis of Landau level spectra and occupation probabilities in various graphene platforms

Fig. 11 illustrates the distinct Landau level across various graphene systems, highlighting fundamental differences in their response to magnetic fields. MLG and BLG exhibit characteristic \sqrt{B} and linear B dependencies respectively, as seen in Eq.(43), while TBG display more complex spectral features. MATBG ($\theta = 1.05^\circ$) shows exceptionally tight level packing resulting from moiré flat band formation, whereas larger twist angles ($\theta = 3.0^\circ$) progressively approach monolayer-like behavior due to interlayer decoupling [35]. These unique Landau level spectra has profound influence over the occupation probabilities as seen in Fig. 12. MATBG's minimal level spacing and low energies enable nearly uniform occupation probability distributions, in contrast to other graphene systems where occupation is more concentrated in lower energy levels due to wider level separations.

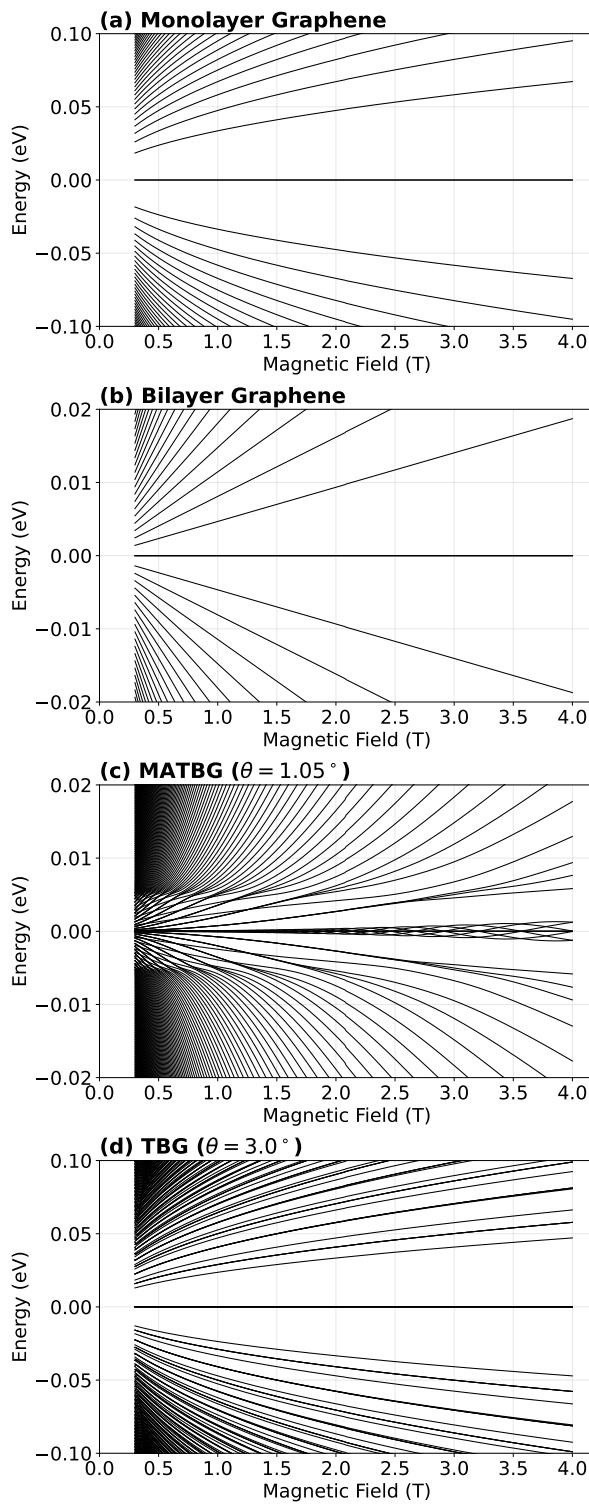


FIG. 11: Magnetic field dependence of Landau level splitting in: (a) MLG, (b) BLG, (c) MATBG at $\theta = 1.05^\circ$, and (d) TBG at $\theta = 3.0^\circ$.

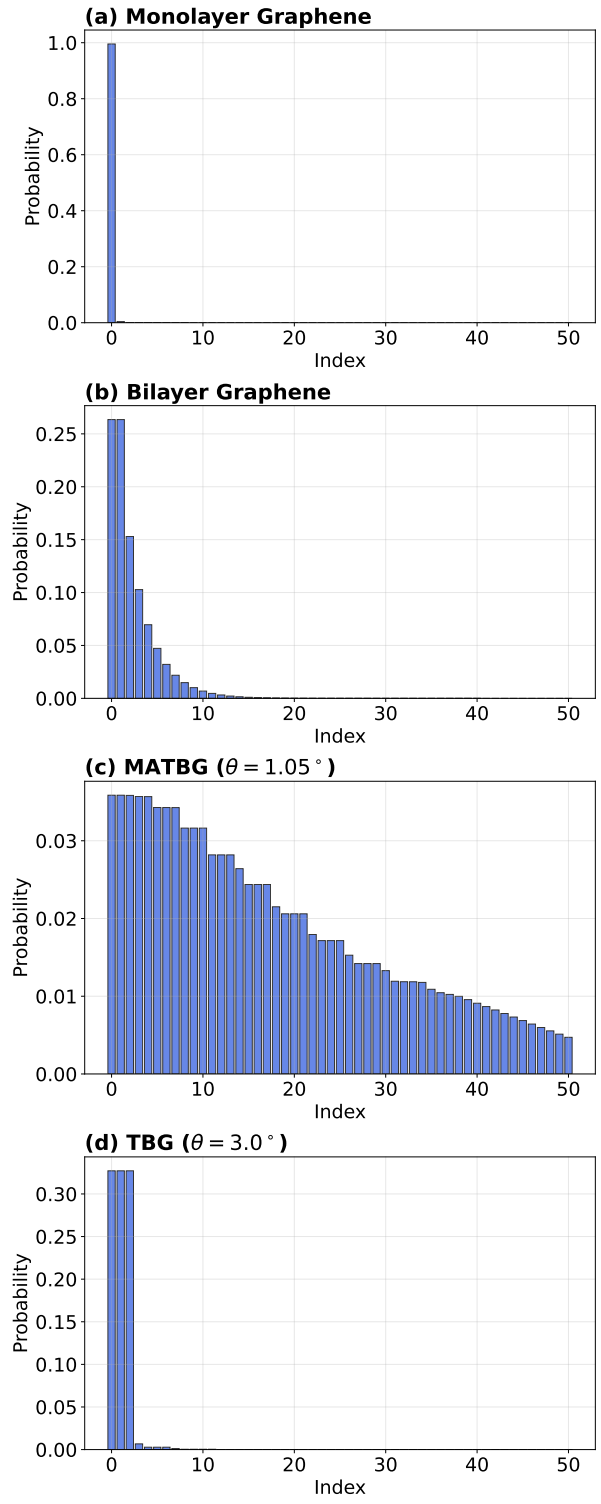


FIG. 12: Occupation probabilities in various graphene platform in thermal equilibrium ($T = 50$ K, $B = 0.5$ T): (a) MLG, (b) BLG, (c) MATBG at $\theta = 1.05^\circ$, and (d) TBG at $\theta = 3.0^\circ$.